Picosecond dynamics of a membrane protein revealed by 2D IR

Prabuddha Mukherjee, Itamar Kass, Isaiah T. Arkin, and Martin T. Zanni

PNAS 2006;103;3528-3533; originally published online Feb 27, 2006;
doi:10.1073/pnas.0508833103

Picosecond dynamics of a membrane protein revealed by 2D IR

Prabuddha Mukherjee[†], Itamar Kass[‡], Isaiah T. Arkin[‡], and Martin T. Zanni[†§]

[†]Department of Chemistry, University of Wisconsin, Madison, WI 53706-1396; and [‡]The Alexander Silberman Institute of Life Sciences, Department of Biological Chemistry, Hebrew University of Jerusalem, Edmund Safra Campus, Givat-Ram, Jerusalem 91904, Israel

Edited by Robin M. Hochstrasser, University of Pennsylvania, Philadelphia, PA, and approved January 10, 2006 (received for review October 8, 2005)

Fast protein dynamics can be missed with techniques that have relatively slow observation times. Using 2D IR spectroscopy and isotope labeling, we have probed the rapid, picosecond dynamics of a membrane protein in its native environment. By measuring the homogeneous and inhomogeneous IR linewidths of 11 amide I modes (backbone carbonyl stretch), we have captured the structural distributions and dynamics of the CD3ζ protein along its transmembrane segment that are lost with slower time-scale techniques. We find that the homogeneous lifetimes and population relaxation times are the same for almost all of the residues. In contrast, the inhomogeneous linewidths vary significantly with the largest inhomogeneous distribution occurring for residues near the N terminus and the narrowest near the center. This behavior is highly consistent with a recently reported experimental model of the protein and water accessibility as observed by molecular dynamics simulations. The data support the proposed CD3ζ peptide structure, and the simulations point to the structural disorder of water and lipid head-groups as the main source of inhomogeneous broadening. Taken together, this rigorous analysis of the vibrational dynamics of a membrane peptide provides experimental insight into a time regime of motions that has so far been largely unexplored.

spectroscopy | ultrafast | vibrational

Since the first structures of proteins became available, it was apparent that protein movement is an essential component of the protein's function. As an example, the oxygen-binding site of myoglobin (1) (the first protein whose structure was solved) is occluded, thereby pointing to necessary movement during the course of the protein's activity. As a result, the scientific community has been developing experimental and computational tools to gain insight into the dynamical aspects of proteins. Most of the experimental techniques developed so far are spectroscopic techniques, because spectroscopic lineshapes depend intimately on fluctuations in molecular structure and the surrounding environments when the dynamical and experimental time scales are comparable (2–4). For example, NMR and ESR are useful probes of slow backbone dynamics and environmentally mediated collision broadening because they probe dynamics on the microsecond-to-millisecond time scale (5–7). Faster time scales are harder to measure with precise structural accuracy, and as a result, most of our knowledge of submicrosecond dynamics comes from molecular dynamics simulations.

In contrast to spin spectroscopies, vibrational spectroscopies probe the picosecond time regime. On this time scale, large structural dynamics appear static (inhomogeneous), whereas fast femtosecond/picosecond structural dynamics, such as fluctuations in hydrogen bonds and solvent dynamics, appear dynamic (spectrally diffusive or homogeneous) (8–10). As a result, the lineshapes of vibrational spectra are sensitive to structural distributions and disorder that is typically averaged out in spectroscopies with slower time resolution. To complement the fast time resolution with good structural resolution, isotopic labeling is used to resolve individual molecular bonds without perturbing the structure.

In principle, both fast and slow dynamics appear in linear IR spectroscopy, but in practice it is impossible to accurately deconvolute linear IR spectra to extract the homogeneous and inhomogeneous distributions that these dynamics generate. In this regard, 2D IR spectroscopy is the tool of choice (11–13). By using a vibrational echo pulse sequence to collect the 2D IR spectra, any inhomogeneous broadening that is present in the system is rephased to create a vibrational echo, whereas the homogeneous distribution is not (14), similar to spin echoes in NMR. As a result, inhomogeneously broadened bands are line-narrowed in 2D IR spectra collected this way, creating peaks that are elongated along the diagonal of the spectra (12, 15, 16). Moreover, by introducing a waiting time into the pulse sequence, structural dynamics on the picosecond time scale are measured by monitoring the 2D lineshape as a function of time that gradually widens because of spectral diffusion (12, 17). In the CD3ζ transmembrane peptide studied here, we find a systematic trend in the elongation of the 2D IR spectra with residue number that correlates to the depth of the residue in the membrane, indicating that the structural disorder of the membrane is reflected in the vibrational lineshapes.

Essential for T cell receptor expression, the human CD3ζ membrane protein is 163 residues long, and its transmembrane segment (residues 31–51), which is α-helical, spans the membrane once (18–20). To obtain residue-level information, we have synthesized and isotopically labeled a 27-residue peptide that encompasses the transmembrane domain. Using 1-$^{13}C{=}^{18}O$ isotope labeling, individual amide I bands along the peptide backbone are frequency-shifted by $\approx$60 cm^{-1}, spectroscopically isolating them from the rest of the peptide (20). In a previous study (20), linear dichroism of 11 labeled residues was measured by using attenuated total reflection Fourier transform IR spectroscopy in oriented lipid bilayers. These measurements gave 11 orientational constraints for the amide I transition dipole relative to the normal of the membrane. The results are consistent with a tetramer transmembrane helical bundle, shown in Fig. 1 (21). The helices were found to be kinked with residues 34L to 39L oriented 18° to the membrane normal and residues 41I to 48A aligned 9° to the normal, forming a funnel-like structure. Taken together, the structural data predict that while both ends of the peptide lie among the lipid headgroups the C terminus is not as exposed to water molecules in comparison to the N terminus, a point that becomes relevant below.

In this article we report a comprehensive 2D IR study encompassing 11 labeled residues spanning the length of the CD3ζ transmembrane helical bundle. For a subset of these residues, we have also determined the population relaxation times and the time scales for spectral diffusion, which are nearly the same for all residues studied. Using the structure of the

Conflict of interest statement: No conflicts declared.

This paper was submitted directly (Track II) to the PNAS office.

Freely available online through the PNAS open access option.

[§]To whom correspondence should be addressed. E-mail: zanni@chem.wisc.edu.

www.pnas.org/cgi/doi/10.1073/pnas.0508833103

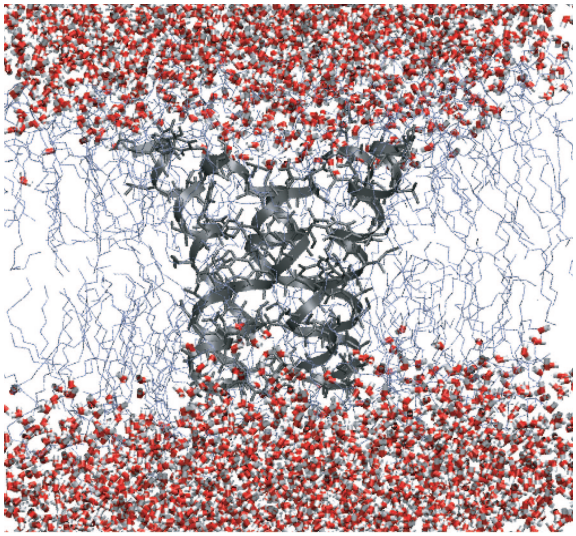

Fig. 1. Proposed structure of the CD3ζ transmembrane peptide bundle (gray). Notice that the bundle is larger at the C-terminal (top) than the N-terminal (bottom) and that the N-terminal is more strongly solvated by water (red) and lipid headgroups (blue).

tetramer transmembrane bundle and recently published methods for calculating amide I frequencies (22), we also ran molecular dynamics trajectories to simulate the data. Comparison of the simulations and experiments confirms the asymmetric structure of the proposed helical bundle and points to the electrostatic field created by water and lipids as the primary cause of linewidth broadening. Besides providing insight into the structural disorder of membrane proteins that is averaged out in spectroscopies with slower time resolution, the results suggest that 2D IR spectroscopy can be used to probe the locations of residues in membrane-bound peptides and proteins based on their level of hydration and proximity to lipid headgroups.

Results

Shown in Fig. 2 *Upper* is the 2D IR spectrum of the 53V-labeled peptide, one of the 11 labeled residues studied here, collected with $t_2 = 0$. Three peaks appear in this spectrum along the diagonal at $\omega_\tau = 1{,}550$, 1,588, and 1,620 cm^{-1}. These correspond to the amide II, the 1-$^{13}C{=}^{18}O$ amide I that is of the primary interest in this article, and the 1-$^{13}C{=}^{16}O$ amide I arising mostly from natural abundance ^{13}C, respectively. The intensities are attenuated outside of the 1,550- to 1,640-cm^{-1} range caused by high optical density of the unlabeled amide I and II bands. By simple inspection, it is apparent that the 1-$^{13}C{=}^{18}O$ peak is very elongated along the diagonal. The photon echo pulse sequence used to collect the 2D IR spectra in this article eliminates the inhomogeneous width along the antidiagonal by rephasing the inhomogeneous distribution to create a vibrational echo in the time domain (14, 16). As a result, homogeneously broadened modes appear nearly round in 2D IR spectra, whereas inhomogeneously broadened modes are elongated along the diagonal. Thus it is clear that the amide I mode of this residue is strongly inhomogeneously broadened.

To extract the 2D lineshape of the labeled amide I mode, we follow our previously established fitting procedure of using the Fourier transform of the third-order response in the limit of Bloch dynamics with a pure dephasing time of T_2^* and an inhomogeneous distribution of Δ_0 (23). The fitting expression in the limit of δ-function pulses is given by

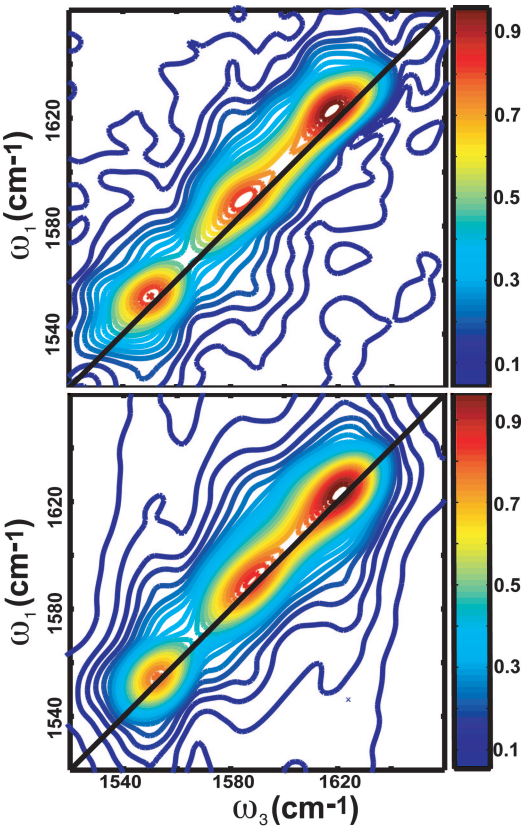

Fig. 2. Absolute value 2DIR spectrum of the isotope label peptide at 53V. (*Upper*) Experimental 2D IR spectrum of the 53V residue. The $^{13}C{=}^{18}O$ amide I band is at $(\omega_1, \omega_3) = (1{,}590\ cm^{-1}, 1{,}588\ cm^{-1})$. (*Lower*) Simulated 2D IR spectra of the same residue using the parameters in Table 1.

$$S(\omega_3,\omega_1) = \left| \int_{-\infty}^{\infty}\int_{-\infty}^{\infty} e^{-i(\omega_1+\omega_3)t} 2|\mu_{10}|^4 e^{-i\omega_{10}\left\{t_3\left(1+\frac{i\Delta}{\omega_{10}}\right)-t_1\right\}} \cdot\left(e^{-t/2T_{10}} - e^{-t/2T_{21}}\right) e^{-\left\{\frac{(t_1+t_3)}{T_2^*}+\frac{\Delta_0^2(t_1-t_3)^2}{2}\right\}} dt_1 dt_3 \right|^2, \quad [1]$$

where ω_{10} is the frequency of the oscillator. T_{10} and T_{21} are the population relaxation times from state $v = 1$ to 0 and 2 to 1, respectively. As shown below, the population relaxation times are nearly the same for all of the residues studied, so we set $T_{10} =$ 600 fs and $T_{21} = 400$ fs (22, 23). We also used an anharmonicity of $\Delta = 14\ cm^{-1}$ (24), the accuracy of which was checked by looking at the negative and positive going peaks in the real parts of the 2D IR spectra (corresponding to the $v = 0$ to 1 and $v =$ 1 to 2 transitions), which match to $<2\ cm^{-1}$ for all of the residues. Explicit pulse widths are used in the actual fitting procedure but have negligible effects on the data. Because the 1-$^{13}C{=}^{18}O$ modes partially overlap with the other two amide modes, for the purpose of lineshape fitting all three bands were included in the simulations with independently varied parameters following Eq. **1**. The simulated 2D IR spectrum of the 53V-labeled peptide is shown in Fig. 2 *Lower*.

This fitting procedure was followed for all 11 labeled peptides. For each of the 11 sites, the sample preparation, collection, and fitting procedure were completed three times for a total of 33 spectra. A representative experimental and simulated 2D IR

Table 1. The diagonal and antidiagonal widths of the $^{13}C{=}^{18}O$ amide I band obtained from fits to the experimental spectra and the corresponding fit parameters

Residue	Diagonal width, cm^{-1}	Antidiagonal width, cm^{-1}	Inhomogeneous distribution, Δ_0 (ps^{-1})	T_2^* time, ps
31Leu	29.0 ± 1.0	15.9 ± 0.5	1.82 ± 0.03	8.0 ± 1.0
34Leu	27.5 ± 0.5	16.8 ± 0.5	1.67 ± 0.03	3.0 ± 0.5
38Iso	26.0 ± 1.0	16.2 ± 0.5	1.55 ± 0.01	10.0 ± 2.0
39Leu	27.0 ± 1.0	18.0 ± 0.5	1.70 ± 0.03	5.0 ± 1.0
41Iso	27.5 ± 0.5	16.2 ± 0.5	1.70 ± 0.03	10.0 ± 2.0
43Gly	27.5 ± 0.5	16.5 ± 0.5	1.65 ± 0.01	5.0 ± 1.0
44Val	25.5 ± 0.5	15.9 ± 0.5	1.55 ± 0.01	5.0 ± 1.0
45Iso	25.0 ± 0.5	14.7 ± 0.5	1.50 ± 0.01	18.0 ± 2.0
46Leu	30.5 ± 0.5	16.2 ± 0.5	2.00 ± 0.03	8.0 ± 1.0
49Leu	31.5 ± 0.5	16.2 ± 0.5	2.10 ± 0.03	16.0 ± 2.0
53Val	32.0 ± 0.5	16.2 ± 0.5	2.10 ± 0.03	15.0 ± 2.0

spectrum for each residue is given in Figs. 8 and 9, which are published as supporting information on the PNAS web site. The results are tabulated in Table 1 with error bars that are set according to the deviations in the three samples and estimates of the systematic errors associated with the fits.

Table 1 reveals several interesting trends. First, the antidiagonal widths are nearly independent of the residue type or position. Except for residues 39L and 45I, the antidiagonal widths all lie within $16+/-1$ cm^{-1}. Because the homogeneous lifetime (T_2) is given by the antidiagonal width, this fact appears to indicate that T_2 is nearly independent of the environment or type of side chain. Second, in stark contrast to the antidiagonal widths, the diagonal widths clearly depend on the position of the labeled residue in the peptide. Plotted in Fig. 3 are the diagonal widths listed in Table 1. Immediately apparent is that the diagonal width systematically varies along the length of the peptide. Overall, there is a 25% change in the diagonal linewidths from the most inhomogeneously broadened amide I bands at the N terminus to the least inhomogeneously broadened band at the 45I position. Furthermore, the trend is not symmetric along the peptide; the onset of inhomogeneous broadening is more rapid at the N terminus than the C terminus and the two ends are not broadened equally. In the middle, residues 41I and 43G are broadened more than their neighbors.

In light of the nearly invariant homogeneous linewidths, we have also measured the population relaxation times of the 34L, 41I, and 49L residues by monitoring the drop in intensity of the 1-$^{13}C{=}^{18}O$ band as a function of the t_2 time, shown in Fig. 4. These three residues reside near the N- and C-terminal ends and in the middle of the peptide at the most homogeneous residue. Within the accuracy of the measurements, these three amide I bands have the same relaxation time, which is $T_{10} \approx 700$ fs when fit with a single exponential decay (solid line in Fig. 4). This value is close to the population relaxation time of the unlabeled amide I band previously measured (23) and the recently measured soluble peptides (25). Considering that the population relaxation times and homogeneous lifetimes are related by $1/T_2 = 1/2T_{10} + 1/T_2^*$ in the Bloch limit, and in light of the fact that the homogeneous lifetimes are nearly the same for all of the residues measured, it appears that the T_{10} time is independent of residue type or position as well. Hence, we conclude that the population relaxation of the amide I mode is intrinsic to the peptide unit itself and depends very little on the surrounding environment or side chains.

The 2D IR spectra above are fit and interpreted assuming that the structural motions can be divided into two categories, fast structural changes that create a homogeneous linewidth and slow structural changes that are so much longer than the IR time scale that they appear static and form an inhomogeneous distribution. To explore structural motions on the IR time scale, we have collected 2D IR spectra of residues 34L, 39L, and 49L for a series of t_2 times spanning 1 ps. The spectra were then fit as above to extract the 2D lineshapes. For these three residues, the 2D lineshapes remain constant to within the experimental resolution. The constant antidiagonal linewidth indicates that there is no measurable amount of spectral diffusion occurring. Thus, Bloch dynamics appears to be a good approximation, indicating that some of the structural fluctuations are fast enough to create

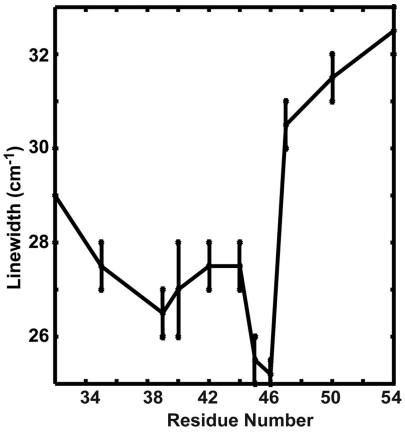

Fig. 3. The diagonal width of the 11 labeled amide I bands taken from Table 1.

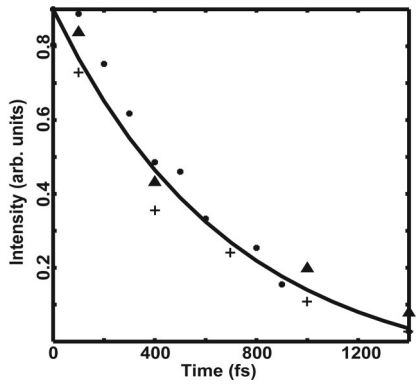

Fig. 4. The population relaxation rates of three different labeled residues [34L (▲), 41I (+), and 49L (●)] and a single exponential decay (solid line) with a time constant of 700 fs.

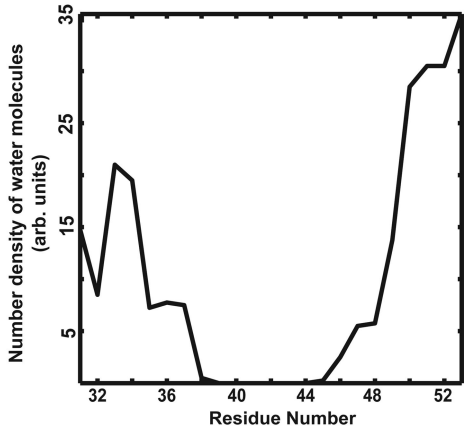

Fig. 5. The number density of the water molecules within a radius of 9 Å from each residue during a 20-ps molecular dynamics run. arb. units, arbitrary units.

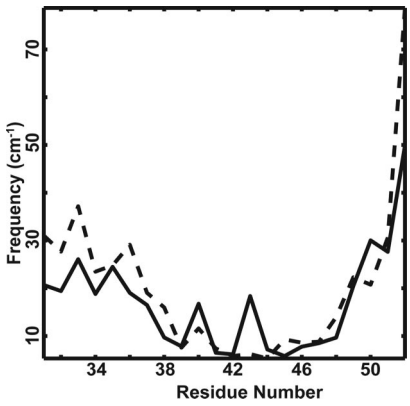

Fig. 6. The standard deviations of the frequency distributions calculated from a 1-ns molecular dynamics run of the peptide bundle. Shown are the individual standard deviations caused by the electrostatic forces of water (solid line) and that caused by lipids (dashed line).

a homogeneous linewidth, but that most of the environment around the peptide remains motionless on the IR time scale.

The structural model for the CD3ζ peptide spans the width of the membrane (Fig. 1), sampling both the polar headgroup regions permeated with water and the highly hydrophobic center of the membrane. Whereas the antidiagonal widths are largely insensitive to the location of the residue in the membrane, the diagonal widths clearly track some aspect of the system that is yet to be identified. The inhomogeneous distributions could be caused by water and lipid headgroups near the terminal ends of the peptide or the broadening could be a reflection of disorder in the peptide structure, which is presumably larger at the ends than in the middle. Determining the cause of the observed trend is one of the main objectives of this article.

Molecular Dynamics Simulations

One of the defining features of the proposed structure for the CD3ζ peptide bundle is its asymmetry in the membrane, closely resembling a funnel structure (20). As described in the Introduction, the C-terminus end projects more steeply into the headgroup region of the membrane surface than the N terminus. As a result, the structural model predicts that the two ends are not evenly hydrated. Shown in Fig. 5 is the level of hydration for each residue calculated by integrating all water molecules in the proposed structure over a sphere of 9 Å centered on each residue during a 20-ps molecular dynamics run. In this plot, the asymmetry of the bundle creates an asymmetry in the water distribution. The similarity of this distribution to the trend in the inhomogeneous distribution (Fig. 3) is remarkable and suggests that there is a direct relationship between the membrane environment and the vibrational dynamics of membrane peptides.

To more quantitatively link the observed trends in the 2D IR linewidths to specific features of the peptide structure and its environment, we have simulated the vibrational frequencies and frequency correlation fluctuations of the amide I bands by using molecular dynamics simulations. Recently, *ab initio* calculations on small peptides in water clusters were used to empirically correlate the amide I frequency to the electrostatic potential or field created by the surrounding solvent environment (22, 26–28). Using the correlation for the field (22) and the structural model for the CD3ζ transmembrane peptide discussed above, we calculated the amide I frequency for every residue in the bundle in 5-fs intervals during a 1-ns trajectory. The frequency shifts caused by water, lipids, and peptides were calculated individually by separately summing their contributions to the electric field.

Of the three components in the system (water, lipids, and peptides), the water and lipids create the largest fluctuations in the frequency. Shown in Fig. 6 are the standard deviations of the amide I frequency distribution for water and lipids. These plots bear a strong resemblance to the data of Fig. 3; they are both minimum in the middle of the peptide and asymmetric. The standard deviations (e.g., the linewidths) are largest at the end of the peptides because the residues become increasingly solvated by water and headgroups near the surface of the membrane. In the middle of the membrane, the electrostatic model predicts that the lipid tails have little effect on the amide I frequencies even though they are highly disordered, but a single water molecule, trapped in the peptide bundle, does cause an increased amount of dephasing at residues 39L and 42Y (Fig. 6) that resembles the data in Fig. 3. The frequency fluctuations caused by the peptides (data not shown) are nearly the same for all residues, because the peptides are α-helical and thus have similar contributions to the electric field at all points along the helix.

Shown in Fig. 7 are the frequency correlation functions $[\langle\omega(t)\omega(0)\rangle]$ for the water, lipid, and peptide that contribute to the amide I band at residue 36D. The frequency correlation function is a measure of how quickly the ensemble of amide I modes dephase, and this function is directly related to IR lineshapes and 2D IR spectra (14). Consider the correlation function described by Bloch dynamics used in Eq. **1**. To describe Bloch dynamics, the correlation function would decay very

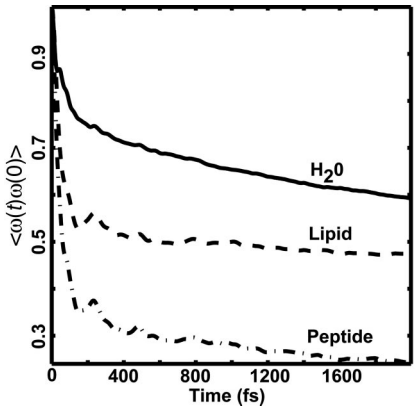

Fig. 7. The frequency fluctuation correlation function of the 31L amide I mode calculated from a 1-ns molecular dynamics run. The correlation functions are calculated separately for the water, lipid, and peptide–peptide electrostatic forces.

rapidly at short times because of fast dephasing from homogeneous broadening and then flatten into a static offset created by a distribution of environments that does not change in time. This picture describes the lipid correlation functions in Fig. 7 extremely well and the peptide correlation moderately well. In effect, the headgroups and peptides do not move much on the IR time scale and thus create offsets in the correlation function that represent their contribution to the inhomogeneous distribution. In contrast, Bloch dynamics is not a good description of the water because its correlation functions decays continuously over 2 ps because of structural dynamics on this time scale. But even at 2 ps the water correlation function still has a large offset because the water distribution, while partly dynamic, remains mostly unchanged (the offset scales roughly with the water concentration near the peptide). Except for the magnitude of the offsets, the water correlation function shown in Fig. 7 is similar for most of the residues, indicating that even though the concentration changes along the peptide, the water dynamics are comparable throughout the membrane and decay on similar time scales to bulk water (29, 30). In comparison, the peptide correlation function tends to decay slower for hydrated residues, whereas for residues in the interior of the membrane it more closely resembles Bloch dynamics.

Discussion

Taken together, the 2D IR data and molecular dynamics simulations provide an in-depth picture of the structural disorder and dynamics of the CD3ζ transmembrane protein segment. The CD3ζ peptide bundle sits in a heterogeneous mixture of water and lipids that is continuously interconverting on a range of time scales. Over the course of a few ps, the 2D IR experiments capture the equilibrium structural ensemble and its dynamics through the frequency fluctuations of the amide I modes. During this time, according to the molecular dynamics simulations, the water, lipids, and peptides all undergo small structural changes that exhibit their forces on the amide I vibrational modes, but the largest contributions to the amide I frequency distributions are created by the static disorder of the system that remains essentially motionless on the IR time scale. This static disorder is presumably created by large structural fluctuations of the peptides and lipids that are too long to be sampled in the short molecular dynamics simulations but have been experimentally characterized with NMR and ESR experiments (31–33). The result is that the 2D IR spectra give a nearly instantaneous snapshot of the ensemble structural distribution.

In principle, the peptides, lipids, and water all contribute to the linewidths, but it is clear from a comparison of the data (Fig. 3) to the standard deviations of the frequencies (Fig. 6) that the 2D IR snapshot primarily captures the heterogeneous distribution of water and lipid headgroups surrounding the protein. These two components have the largest effect on the frequency distributions because they have large dipoles (and charges) that interact strongly with the amide groups. While also highly disordered, the lipid chains do not significantly contribute to the linewidths because they are nonpolar. Likewise, the peptides contribute little to the linewidths because their fields are less than half that of the water or headgroups. The trends may be different for soluble peptides with more uniform water coverage or for other secondary structures. In fact, a $^{13}C{=}^{18}O$ 2D IR study on four residues near the middle of a soluble α-helix was recently reported by Fang and Hochstrasser (25). They observed a $\approx$1-cm^{-1} difference in linewidths, which they attributed to side-chain interactions, and a slight amount of spectral diffusion during the first 200 fs. Like us, they found that the population relaxation (T_1 = 525 fs) did not depend on residue position. Comparison between membrane and soluble peptides is a promising approach for unraveling the environmental and structural contributions to the dynamical linewidths.

Although the data and simulations reported here are very similar, the comparison is not quantitative. This difference could be caused by an incomplete structural model, which was developed without structural constraints for the depth of the peptides in the membrane or interhelix distances (20). Another consideration is that the empirical correlation between electric field strength and amide I frequency was developed by using a model amide unit, *N*-methylacetamide, solvated in bulk water (22). Because the electric field strengths on the amide units in the hydrophobic interior of the membrane are much smaller than in bulk water, the correlation may not be rigorous. Furthermore, our analysis did not account for motional narrowing, which may explain why the homogeneous widths are invariant to water concentration. Regardless of these uncertainties, it should be noted that the trend in the experimental data strongly support an asymmetric structure for the peptide bundle and that improvements in the simulations will lead to more accurate interpretation of the experimental data.

It is interesting to note that the experimental data in Fig. 3 showed a pronounced increase in dephasing rate for residues 44V and 45I, but the molecular dynamics simulations find that the only appreciable source of dephasing in the middle of the helix arises from a single water molecule trapped in the helix bundle (Fig. 6). The statistical significance of this water molecule is not known, and limitations of the model discussed above might overestimate the effect of the water molecule on the electric field fluctuations. But the observation suggests that the frequency fluctuations of amino acids that line the pores in channel proteins might be comparable to the fluctuations of residues partially solvated in the headgroup region.

Conclusions

In this study we find that the picosecond dynamics of membrane peptides create 2D IR linewidths that are sensitive to the surrounding distribution of water and lipid headgroups. In contrast, the homogeneous linewidths and population relaxation times are mostly independent of the environment and are probably intrinsic to the amide I unit itself. Although much work needs to be done to better understand how vibrational dynamics depend on environment and how to predict linewidths from molecular dynamics simulations, our results suggest that 2D IR spectroscopy and amide I isotope labeling can be used as a noninvasive way to explore the structures and dynamics of membrane peptides and proteins. For example, our results suggest that IR linewidths should be significantly different for residues that line the pores of channel proteins versus residues facing the hydrophobic membrane interior. Although not explored here, a natural complement to IR linewidths are vibrational couplings that are sensitive to structure. In fact, in our previous report (23) we observed cross peaks caused by coupling between the peptides and lipid headgroups that might also be used as structural markers, a signature that Volkov and Hamm (34) have also recently observed for a membrane-bound tripeptide. Other advantages of 2D IR spectroscopy include small sample requirements ($<$10 nmol of sample are needed) and fast time resolution. This article focuses on equilibrium structures, but a natural extension would be to use 2D IR linewidths to follow protein insertion into membranes on a submillisecond time scale.

Materials and Methods

Materials. Isotopically labeled 1-$^{13}C{=}^{18}O$ membrane peptides were synthesized as described (20). The peptides were 27 aa long and had the sequence DPKL*GYL*LDGI*L*FI*YG*V*I*L*TAL*FLRV*K that spans residues 28–54 of the CD3ζ protein. A separate sample was synthesized for each isotope label (X*). In a 1:15 ratio, the peptides and dimyristoylphosphocholine were dissolved in deuterated hexafluoroisopropanol to

deuterate all of the labile protons. The samples were dried, and D_2O was added with a temperature maintained between 30°C and 35°C to ensure formation of bilayer vesicles in the lamellar phase. To collect the spectra, the membrane peptide samples were held between two CaF_2 plates separated by 56 μm. The optical density of the 1-$^{13}C{=}^{18}O$ peak (which was synthesized with ≈75% efficiency) was ≈0.05, and those of amide I and II were ≈3.4 and 1.3, respectively. There was no background in the region of the isotope label (23).

2D IR Method. The experimental procedure for collecting heterodyned 2D IR spectra has been described (35). In brief, three fs Fourier transform limited pulses (1.2 μJ, 150-cm^{-1} bandwidth, 400 nJ) with wavevectors k_1, k_2, and k_3 were incident on the sample and the signal was monitored in the $-k_1 + k_2 + k_3$ phase-matching direction with a fourth local oscillator pulse (≈2 nJ) that measured the time dependence of the emitted signal in a balanced heterodyne detection system. All four pulses had identical polarizations. The time delay between pulses in the directions k_1 and k_2 was t_1, between k_2 and k_3 it was t_2, and between k_3 and the local oscillator pulse it was t_3. The 2D IR data set was generated by collecting the heterodyned signal as a function of t_3 and t_1, both of which were scanned 2,500 fs in 18-fs steps for a fixed t_2. The 2D IR spectra were generated by Fourier-transforming the time-domain data along t_1 and t_3, and the absolute value of the Fourier-transformed spectra are reported. The translation stages used to generate the spectra were calibrated to within ± 2 cm^{-1}.

Molecular Dynamics. The left-handed tetrameric structural model of CD3ζ peptide previously reported (spanning residues 31–51) was used as the starting point for the simulations here (21). Using the GROMACS (36, 37) software package, the gas-phase protein structure was inserted into the lipid bilayer following the protocol described (38), and the system was equilibrated for 10 ns. The equilibration was followed by a 1-ns production run by using 0.5-fs time steps. We used particle mesh Ewald (PME) for the electrostatics and SHAKE for constraining the bonds. The coordinates and the electrostatic forces on each of the atoms of the protein molecules were saved every 5 fs, and the quantities were converted to the amide I frequencies by using the parameters of Schmidt *et al.* (22), from which the correlation function and standard deviations were calculated.

M.T.Z. and P.M. thank J. R. Schmidt and J. Skinner for helpful discussions. This research was supported by the Beckman Foundation and National Institutes of Health Grant 1R21AI064797-01. I.T.A. was supported by Israel Science Foundation Grant 784/01.

1. Kendrew, J. C. (1963) *Science* **139,** 1259–1266.
2. Kubo, R. (1969) *Adv. Chem. Phys.* **15,** 101–127.
3. Berne, B. J. & Pecora, R. (1976) *Dynamic Light Scattering* (Wiley, New York).
4. Oxtoby, D. W., Levesque, D. & Weis, J.-J. (1978) *J. Chem. Phys.* **68,** 5528–5533.
5. Cavanagh, J., Fairbrother, W. J., Palmer, A. G., III & Skelton, N. J. (1996) *Protein NMR Spectroscopy: Principles and Practice* (Academic, New York).
6. Lietzow, M. A. & Hubbell, W. L. (1998) *Biophys. J.* **74,** A278–a278.
7. Dyson, H. J. & Wright, P. E. (2005) *Nuclear Magn. Reson. Biol. Macromolecules C* **394,** 299–321.
8. Zimdars, D., Tokmakoff, A., Chen, S., Greenfield, S. R., Fayer, M. D., Smith, T. I. & Schwettman, H. A. (1993) *Phys. Rev. Lett.* **70,** 2718–2721.
9. Hamm, P., Lim, M. & Hochstrasser, R. M. (1998) *Phys. Rev. Lett.* **81,** 5326–5329.
10. Hamm, P. & Hochstrasser, R. M. (2001) *Ultrafast Infrared and Raman Spectroscopy* (Dekker, New York).
11. Asplund, M. C., Zanni, M. T. & Hochstrasser, R. M. (2000) *Proc. Natl. Acad. Sci. USA* **97,** 8219–8224.
12. Zanni, M. T., Gnanakaran, S., Stenger, J. & Hochstrasser, R. M. (2001) *J. Phys. Chem. B* **105,** 6520–6535.
13. Golonzka, O., Khalil, M., Demirdöven, N. & Tokmakoff, A. (2001) *Phys. Rev. Lett.* **86,** 2154–2157.
14. Mukamel, S. (1995) *Principles of Nonlinear Spectroscopy* (Oxford Univ. Press, New York).
15. Tokmakoff, A. (2000) *J. Phys. Chem. A* **104,** 4247–4255.
16. Zanni, M. T., Asplund, M. C. & Hochstrasser, R. M. (2001) *J. Chem. Phys.* **114,** 4579–4590.
17. Demirdoven, N., Khalil, M. & Tokmakoff, A. (2002) *Phys. Rev. Lett.* **89,** 237401.
18. Manolios, N. (1995) *Immunol. Cell Biol.* **73,** 544–548.
19. Jacobs, H. (1997) *Immunol. Today* **18,** 565–569.
20. Torres, J., Briggs, J. A. G. & Arkin, I. T. (2002) *J. Mol. Biol.* **316,** 365–374.
21. Torres, J., Briggs, J. A. G. & Arkin, I. T. (2002) *J. Mol. Biol.* **316,** 375–384.
22. Schmidt, J. R., Corcelli, S. A. & Skinner, J. L. (2004) *J. Chem. Phys.* **121,** 8887–8896.
23. Mukherjee, P., Krummel, A. T., Fulmer, E. C., Kass, I., Arkin, I. T. & Zanni, M. T. (2004) *J. Chem. Phys.* **120,** 10215–10224.
24. Fang, C., Wang, J., Charnley, A. K., Barber-Armstrong, W., Smith, A. B., III, Decatur, S. M. & Hochstrasser, R. M. (2003) *Chem. Phys. Lett.* **382,** 586–592.
25. Fang, C. & Hochstrasser, R. M. (2005) *J. Phys. Chem. B* **109,** 18652–18663.
26. Ham, S., Kim, J. H., Lee, H. & Cho, M. H. (2003) *J. Chem. Phys.* **118,** 3491–3498.
27. Choi, J. H., Ham, S. Y. & Cho, M. (2003) *J. Phys. Chem. B* **107,** 9132–9138.
28. Bour, P. & Keiderling, T. A. (2003) *J. Chem. Phys.* **119,** 11253–11262.
29. Fecko, C. J., Eaves, J. D., Loparo, J. J., Tokmakoff, A. & Geissler, P. L. (2003) *Science* **301,** 1698–1702.
30. Asbury, J. B., Steinel, T., Kwak, K., Corcelli, S. A., Lawrence, C. P., Skinner, J. L. & Fayer, M. D. (2004) *J. Chem. Phys.* **121,** 12431–12446.
31. Bocian, D. F. & Chan, S. I. (1978) *Annu. Rev. Phys. Chem.* **29,** 307–335.
32. Nevzorov, A. A. & Brown, M. F. (1997) *J. Chem. Phys.* **107,** 10288–10310.
33. Ge, M. T. & Freed, J. H. (2003) *Biophys. J.* **85,** 4023–4040.
34. Volkov, V. & Hamm, P. (2004) *Biophys. J.* **87,** 4213–4225.
35. Fulmer, E. C., Mukherjee, P., Krummel, A. T. & Zanni, M. T. (2004) *J. Chem. Phys.* **120,** 8067–8078.
36. Berendsen, H. J. C., Vanderspoel, D. & Vandrunen, R. (1995) *Comput. Phys. Commun.* **91,** 43–56.
37. Lindahl, E., Hess, B. & van der Spoel, D. (2001) *J. Mol. Model.* **7,** 306–317.
38. Faraldo-Gomez, J. D., Smith, G. R. & Sansom, M. S. P. (2002) *Eur. Biophys. J. Biophys. Lett.* **31,** 217–227.

Corrections

CELL BIOLOGY. For the article "Breast cancer bone metastasis mediated by the Smad tumor suppressor pathway," by Yibin Kang, Wei He, Shaun Tulley, Gaorav P. Gupta, Inna Serganova, Chang-Rung Chen, Katia Manova-Todorova, Ronald Blasberg, William L. Gerald, and Joan Massagué, which appeared in issue 39, September 27, 2005, of *Proc. Natl. Acad. Sci. USA* (**102,** 13909–13914; first published September 19, 2005; 10.1073/pnas.0506517102), the authors note that "Fig. 2*B* shows SCP3 cells transduced with a vector constitutively expressing red fluorescent protein (RFP, *Upper*) and a vector expressing green fluorescent protein (GFP) under the control of a TGF-β responsive promoter (*Lower*). An erroneous, unpaired set of images was used in the +TGF-β panels of the previously published version of this figure." The corrected figure and its legend appear below. This correction does not affect the conclusions of the article.

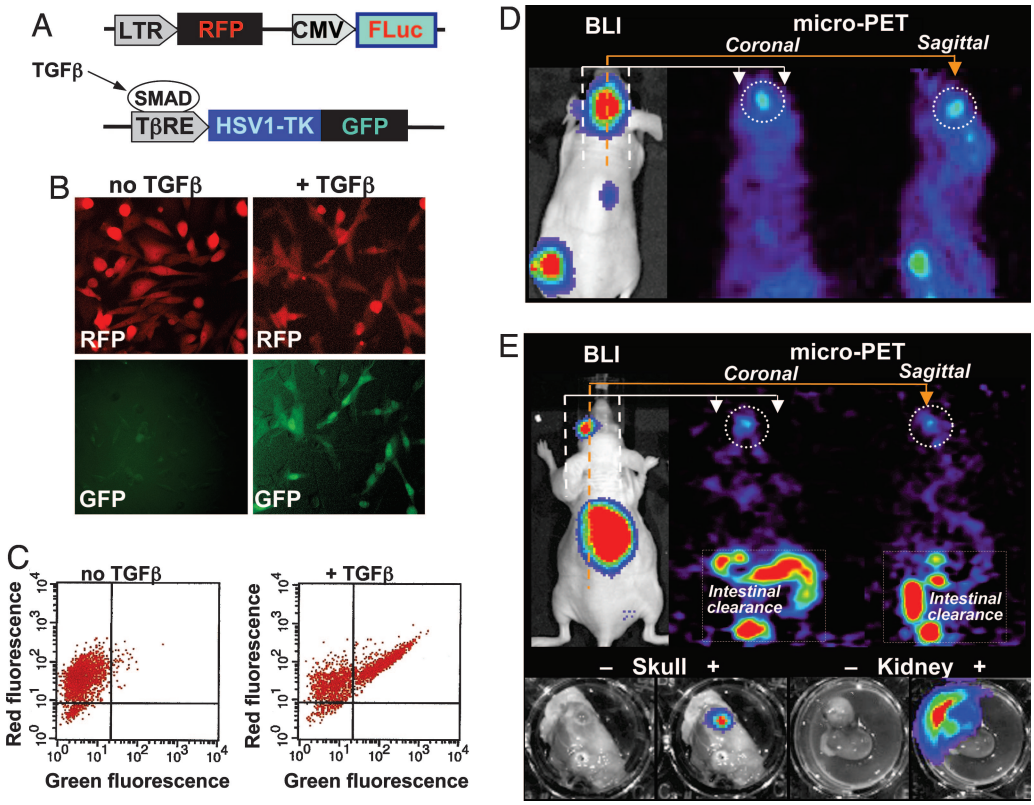

Fig. 2. Functional imaging of Smad signaling in breast cancer bone metastasis. (*A*) Schematic representation of the retroviral vectors SFG-tdRFP-cmvFLuc (constitutively expressing tdRFP and FLuc) and *cis*-TGF-β1–Smads–HSV1-tk/GFP (expressing HSV-tk/GFP fusion protein in response to TGF-β). (*B* and *C*) SCP3 transduced with these two vectors were treated with TGF-β or no additions for 24 h and analyzed by fluorescence microscopy (*B*) or two-color FACS (*C*). The constitutive tdRFP fluorescence is shown on the ordinate, and the HSV-tk/GFP fusion fluorescence, inducible by TGF-β, is shown on the abscissa. (*D* and *E Upper*) *In vivo* bioluminescence and microPET imaging of metastases in mice. SCP2 (*D*) and SCP3 (*E Upper*) cells bearing the SFG-tdRFP-cmvFLuc and *cis*-TGF-β1–Smads–HSV1-tk/GFP vectors were injected into the left cardiac ventricle and analyzed after 4 weeks (SCP2) or 18 weeks (SCP3). Bioluminescence imaging shows sites of metastases in the skull (*D* and *E*) and adrenal gland (*E Upper*). ^{18}F-2′-fluoro-2′deoxy-1β-D-arabionofuranosyl-5-ethyl-uracil microPET images of tk/GFP reporter activation shows localization of radioactivity to the skull in the coronal and sagittal image planes. No visualization of the adrenal metastasis was seen on microPET imaging. Note the nonspecific accumulation of the tracer in the gastrointestinal tract and bladder attributable to clearance of the tracer. (*E Lower*) At necroscopy, the head showing the skull and the adrenal metastasis plus kidney were removed and imaged *ex vivo* for photographic (−) and bioluminescence (+) imaging.

www.pnas.org/cgi/doi/10.1073/pnas.0603221103

CHEMISTRY. For the article "Picosecond dynamics of a membrane protein revealed by 2D IR," by Prabuddha Mukherjee, Itamar Kass, Isaiah Arkin, and Martin T. Zanni, which appeared in issue 10, March 7, 2006, of *Proc. Natl. Acad. Sci. USA* (**103,** 3528–3533; first published February 27, 2006; 10.1073/pnas.0508833103), the author name Isaiah Arkin should have appeared as Isaiah T. Arkin. The online version has been corrected. The corrected author line appears below.

Prabuddha Mukherjee, Itamar Kass, Isaiah T. Arkin, and Martin T. Zanni

www.pnas.org/cgi/doi/10.1073/pnas.0602988103